Research Article Vol. 61, No. 24 / 20 August 2022 / Applied Optics 6961

applied optics

Alleviated built-in electric field in the active region of AlGaN deep-ultraviolet light-emitting diodes with locally embedded p-i-n junctions

YONGCHEN JI,[1] MENGRAN LIU,[1,2] AND CHAO LIU[1,2,*]

[1]School of Microelectronics, Institute of Novel Semiconductors, Shandong Technology Center of Nanodevices and Integration, State Key Laboratory of Crystal Materials, Shandong University, Jinan 250100, China
[2]Shenzhen Research Institute, Shandong University, Shenzhen 518057, China
*Corresponding author: chao.liu@sdu.edu.cn

Received 17 May 2022; revised 25 July 2022; accepted 26 July 2022; posted 28 July 2022; published 11 August 2022

The strong polarization-induced electric field in the multi-quantum well region reduces the radiative recombination rates by separating the electron and hole wave functions, which is one of the most detrimental factors that is to blame for the low luminous efficiency of AlGaN deep-ultraviolet light-emitting diodes (DUV LEDs). In this work, we redesigned the active region by incorporating Si and Mg doping at the vicinity of the quantum wells, forming a series of embedded $p-i-n$ junctions in the multi-quantum well region. The additional electric field induced by the fixed charges from the embedded doping-induced junctions can effectively compensate for the intrinsic polarization-induced electric fields in the quantum well region and give rise to the improved overlap of hole and electron wave function, hence enhancing the radiative recombination rates and the external quantum efficiency and optical power of DUV LEDs. The mechanism behind the alleviated polarization electric field is comprehensively discussed and analyzed. The embedded $p-i-n$ junctions can also alter the band diagram structure of the active region, decrease the effective barrier heights for holes, and diminish the electron leakage into the p-type region. In addition, different thicknesses and doping concentrations of the embedded p- and n- layers were designed, and their influence on the performance of DUV LEDs was numerically analyzed. The proposed structure with embedded $p-i-n$ junctions provides an alternative way to achieve efficient DUV LEDs. © 2022 Optica Publishing Group

https://doi.org/10.1364/AO.464029

1. INTRODUCTION

AlGaN deep-ultraviolet light-emitting diodes (DUV LEDs) have demonstrated great potential in medical disinfection, water and air purification, and microelectronic photolithography [1–5]. Pandemics like COVID-19 have caused increasing demands for DUV LEDs in public health disinfection systems. However, the optical power and external quantum efficiency (EQE) of AlGaN-based DUV LEDs are far from satisfactory in the current stage and a high-efficiency DUV LED is highly desirable to replace mercury-based light sources.

A number of factors are responsible for the poor optical and electrical performance of DUV LEDs, such as the low hole injection efficiency [6,7] and serious electron leakage [8,9]. Numerous structures were proposed and investigated to resolve the aforementioned carrier transport problems, and extensive efforts have been devoted to modifying the structure of the electron blocking layer (EBL) and its immediate vicinity, such as $p-$AlGaN/AlGaN/$p-$AlGaN EBL [10], Al composition linearly grading EBL [11], last quantum barrier (LQB) with linearly increased Al composition [12], and particularly doped LQB [13]. Besides, different structures inserted between EBL and LQB have also been proved to effectively boost the light output power (LOP) [14,15]. Recently, we found that by incorporating a polarization-engineered AlxGa1-xN/AlyGa1-yN superlattice layer at the EBL/LQB interface, the polarization charge type can be inverted from positive to negative and the hole injection efficiency can be enhanced effectively [16].

Other than the carrier transport issue, the low radiative recombination rates in the active region are another nonnegligible issue that directly determines the luminous efficiency of DUV LEDs and urgently remains to be solved. On the one hand, the crystalline quality of the multiple quantum wells (MQWs) grown along the [0001] orientation can directly affect the radiative recombination rates and LOP [17–19]. Growing underlayer and superlattices below the MQWs can efficiently reduce the concentration of deep traps and nonradiative recombination centers in quantum wells (QWs) [20,21]. On the other hand, the large lattice mismatch between the QWs and the quantum barriers (QBs) arouses a strong polarization-induced electric field, which leads to a spatial separation of

carrier wave function and decreases the luminous efficiency [22,23]. Some unique methods were proposed to alleviate the polarization electric field and boost the radiative recombination rates in the active region of DUV LEDs. The overlap of wave function for electrons and holes can be improved effectively by taking advantage of the Al composition-graded QBs [24]. Quaternary AlInGaN barriers have also been utilized to suppress the polarization-induced electric field [25]. Additionally, DUV LEDs grown on large misoriented sapphire substrates have been reported with increased wave function overlap of carriers and enhanced radiative recombination [26]. In addition, there are also reports demonstrating that Si doping in QBs is effective in improving the forward electrical performance of DUV LEDs [27,28]. Nevertheless, there has been no report on modulating the built-in electric field by engineering the doping profile in the active region, and the mechanism behind the alleviated polarization electric field simply through doping in QBs in DUV LEDs remains to be explored and investigated.

In this paper, we propose an alternative approach toward screening the polarization-induced electric field in the active region of AlGaN DUV LEDs. By implementing MQWs with locally embedded $p-i-n$ junctions, the extra donors and acceptors can partially compensate for the polarization charges at the QW/QB interface, contributing to a reduced overall electric field in QWs. Thus, enhanced radiative recombination rates and LOP can be obtained in comparison with the reference sample. Furthermore, the optical and electrical characteristics of DUV LEDs with different doping thicknesses and concentrations in the QBs are numerically compared and studied. The physical mechanism behind the enhanced performance of the proposed DUV LEDs is comprehensively investigated.

2. DEVICE STRUCTURE AND PARAMETERS

Figure 1(a) depicts the epitaxial structure of the DUV LEDs in this study, which consists of a 4 μm-thick $n-Al_{0.6}Ga_{0.4}N$ with an electron concentration $8\times10^{18}\ cm^{-3}$, five periods of $Al_{0.45}Ga_{0.55}N/Al_{0.57}Ga_{0.43}N$ MQWs (the thicknesses of each $Al_{0.45}Ga_{0.55}N$ QW and $Al_{0.57}Ga_{0.43}N$ QB are 3 nm and 10 nm, respectively) as the active region, a 10 nm-thick $p-Al_{0.6}Ga_{0.4}N$ EBL, a 50 nm-thick $p-Al_{0.4}Ga_{0.6}N$ hole supplier, and a 50-nm-thick p-GaN cap layer. The effective hole concentrations of p-type layers are set to be $\sim1\times10^{17}\ cm^{-3}$. The mesa size of the DUV LED structures is set to be 350 μm × 350 μm. Figures 1(b) and 1(c) schematically show the design of the active region, in which the QWs and QBs of the reference sample (denoted as Device A) remain undoped while a series of $p-i-n$ junctions are locally incorporated at the vicinity of each QW for the proposed structure (denoted as Devices B to D). Specially, for Devices B to D, the green region in QBs is doped by Mg, while the yellow region in QBs is doped by Si, as shown in Figs. 1(b) and 1(c), which forms an embedded $p-i-n$ junction for the purpose of modulating the built-in electric field of the active region. Correspondingly, the Al composition of the p-type and n-type region is 57%, identical to that of the QBs, while the intrinsic region of the embedded $p-i-n$ junctions features an Al composition of 45%, the same as that of the QWs. To explore the influence of the embedded $p-i-n$ junctions on the performance of the DUV LEDs,

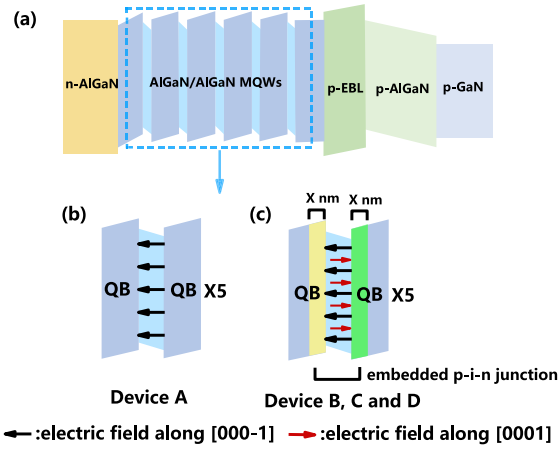

Fig. 1. (a) Schematic diagrams of the reference sample (denoted as Device A). Structures in MQWs region of (b) Device A, (c) Devices B, C, and D. The polarization electric field in QWs has been marked by black arrows, while the electric field produced by embedded $p-i-n$ junctions has been marked by red arrows.

the doping thickness (x) and doping concentration are varied from Device B to Device D. The value of x is set as 2 nm and the Mg and Si doping concentrations are both $2\times10^{18}\ cm^{-3}$ for Device B. The value of x is increased to 3 nm in Device C, with a doping concentration identical to that of Device B. The doping concentration of Mg and Si in Device D are both increased to $5\times10^{18}\ cm^{-3}$, and the value of x is the same as Device C.

The numerical investigation was conducted by using the Advanced Physical Models of Semiconductor Devices (APSYS) software, which can self-consistently solve Schrödinger and Poisson's equations with proper boundary conditions. Drift-diffusion equations and material parameters for III-nitride semiconductors are taken into account during the numerical simulation process [29,30]. The built-in interface charges caused by the spontaneous and piezoelectric polarization are calculated based on the theory proposed by Fiorentini *et al.* [31]. The possible defect factors have been taken into account, and the interfacial charge density is assumed to be 40% of the theoretical value [32]. The Shockley–Read-Hall (SRH) recombination lifetime, light extraction efficiency, and auger recombination coefficient are set to be 14 ns, 6%, and $1.7\times10^{-30}\ cm^6/s$, respectively. Similar values can be found in Refs. [15,33–35], validating the accuracy and rationality of our simulation. What is more, a band offset ratio of the AlGaN/AlGaN heterojunctions is set as 50:50, which is defined as the ratio between the conduction band offset and valence band offset [36].

3. RESULTS AND DISCUSSION

The calculated L-I-V and EQE curves are plotted in Figs. 2(a) and 2(b), respectively. The numerically calculated LOP and EQE values (black curves) of Device A are consistent with the experimentally measured data (red dots) from Ref. [37], suggesting the effectiveness of our device model and parameters adopted in the calculation. At a current density of $170\ A/cm^2$, the LOP of Devices A, B, C, and D is $16.72\ W/cm^2$,

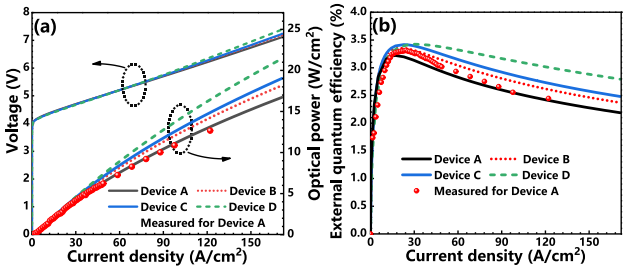

Fig. 2. Calculated (a) L-I-V characteristic, and (b) EQE for Devices A, B, C, and D in terms of the injection current.

18.17 W/cm^2, 19.03 W/cm^2, and 21.43 W/cm^2, respectively. Compared with the reference sample, the LOP of Device D is increased by 28%, and the efficiency droop is significantly reduced by 42.51% at a current density of 170 A/cm^2. Nearly the same forward voltages have been observed in the four devices, indicating that the DUV LEDs with embedded $p-i-n$ junctions can generate higher LOP with nearly the same power consumption compared with the reference sample.

To explore the effect of the embedded $p-i-n$ junctions on reducing the built-in electric field, we extracted the electric field in the active region of the four investigated devices at an injection current density of 110 A/cm^2, as shown in Fig. 3(a). We also plotted the electric field profiles of the last QW in Fig. 3(b) for an explicit exhibition. For the reference Device A, a negative built-in electric field of around -4×10^5 V/cm can be observed in the active region, which indicates that the overall electric field in the active region is in the opposite direction of the [0001] growth orientation, resulting in spatial separation of the electron/hole wave functions and thus reduced recombination efficiency of the LEDs. With incorporated $p-i-n$ junctions in the active region of Device B, a remarkable reduction can be recorded in the overall electric field of the active region, thanks to the combined effect of the electric field induced by the $p-i-n$ junction and the polarization-induced electric field due to the lattice mismatch between the QW and QB layers. To figure out the influence of the doping concentration and thickness on modulating the built-in electric field, we first increased the doping thickness from 2 nm in Device B to 3 nm in Device C while keeping the doping concentration unchanged, and then increased the doping concentration from 2×10^{18} cm^{-3} in Device C to 5×10^{18} cm^{-3} in Device D while keeping the thickness identical. It can be seen that only a minor reduction can be observed from Device B to Device C, while the electric field is dramatically reduced from Device C to Device D, indicating the doping concentration possesses the most significant impact on the reduction of the overall built-in electric field in the active region.

For the purpose of revealing the mechanism behind the reduction of the overall electric field in the active region, we established an analytical model by calculating the polarization charges and fixed charges-induced electric fields at the QW/QB interfaces. As schematically depicted in Fig. 3(c), the electric fields induced by the fixed charges possess opposite directions and thus can be utilized to compensate for the intrinsic electric fields induced by the polarization charges at the hetero QW/QB interfaces.

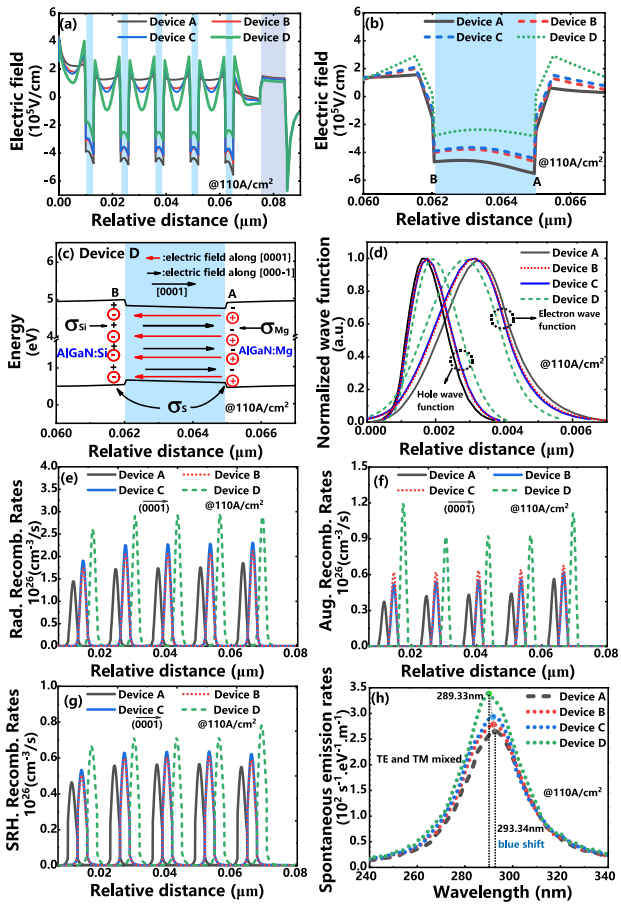

Fig. 3. Electric field in (a) MQWs region, p-EBL, and part of $p-Al_{0.4}Ga_{0.6}N$, and (b) the last QW of all investigated devices; (c) calculated energy band diagram and charge distribution in Device D; (d) normalized electron and hole wave function in the last QW for Devices A, B, C, and D; (e) radiative recombination rates; (f) Auger recombination rates; and (g) SRH recombination rates in the MQWs. For a clear comparison, the horizontal positions of three recombination rates for Devices B, C, and D are artificially shifted by 3, 3, and 6 nm, respectively, compared with Device A. The data are all extracted at the injection current density of 110 A/cm^2. (h) Total spontaneous emission rates of the four DUV LEDs.

The polarization charges-induced electric fields at both interface A and B can be expressed by the following equation:

$$\left|\vec{E}_{sp+pz}\right| = \frac{e\sigma_s}{\varepsilon_r\varepsilon_0}, \tag{1}$$

where e is the elementary electronic charge, σ_s is denoted as the density of the polarization-induced charges, ε_r is the relative dielectric constant of AlGaN, and ε_0 is the electric permittivity in vacuum.

The fixed charges-induced electric fields at interface A and B are related to the ionized Mg and Si impurities in the $p-i-n$ embedded junctions, respectively, which can be expressed by the equations below,

$$\left|\vec{E}_{Mg}\right| = \frac{e\sigma_{Mg}}{\varepsilon_r\varepsilon_0}, \tag{2}$$

$$\left|\vec{E}_{Si}\right| = \frac{e\sigma_{Si}}{\varepsilon_r\varepsilon_0}, \tag{3}$$

where σ_{Mg} is the density of the ionized Mg impurities and can be obtained from $\sigma_{Mg} = p_D^+ \times t_D$, where p_D^+ is the concentration of the ionized Mg acceptor and t_D is the thickness of ionized acceptor region in each QB. σ_{si} is the density of the ionized Si impurities and can be obtained from $\sigma_{si} = n_D^+ \times t_D$, where n_D^+ is the concentration of the ionized Si donor and t_D is the thickness of ionized donor region in each QB.

It should be noted that only polarization charges-induced electric fields are considered in the reference Device A, while Devices B to D also involve the electric fields induced by the fixed charges from the embedded $p-i-n$ junctions. Therefore, the overall electric field in the QW region at interface A for Devices B to D can be expressed by

$$\left|\vec{E}_{sp+pz} + \vec{E}_{Mg}\right| = \frac{e|\sigma_s - \sigma_{Mg}|}{\varepsilon_r \varepsilon_0}. \tag{4}$$

Similarly, the overall electric field at interface B can be calculated by

$$\left|\vec{E}_{sp+pz} + \vec{E}_{Si}\right| = \frac{e|\sigma_s - \sigma_{Si}|}{\varepsilon_r \varepsilon_0}. \tag{5}$$

By analyzing the equations above, it can be deduced that the fixed charges-induced electric fields in the embedded $p-i-n$ junctions can reasonably compensate for the intrinsic polarization charges-induced electric fields, which can verify the effectiveness of the proposed structures.

The electron and hole wave functions of Devices A, B, C and D are plotted in Fig. 3(d). The wave function overlap (Γ_{e-hh}) of Devices A, B, C, and D comes in increasing patterns, which are calculated to be 42.42%, 54.23%, 56.58%, and 75.66%, respectively. The dramatically enhanced Γ_{e-hh} for Devices B, C, and D is attributed to the reduction of electric fields in the active region and can benefit the recombination of electrons and holes in the QW regions.

The radiative, Auger, and SRH recombination rates of all the studied devices are displayed in Figs. 3(e), 3(f), and 3(g), respectively. With suppressed built-in electric field and increased wave function overlap, Devices B, C, and D are featured with boosted radiative recombination rates as well as enhanced nonradiative recombination rates [38,39]. With the combined effects from the recombination processes above, Device D features the highest peak spontaneous emission rates, which is 27.7% higher than that of Device A, indicating an effective improvement in the luminous characteristics of the DUV LEDs with embedded $p-i-n$ junctions. Moreover, the peak emission wavelength of Device D exhibits a blueshift of ~ 4 nm, which is attributed to the alleviated quantum confined Stark effect (QCSE) under the circumstances of the reduced electric field in the QW regions [40–43]. Other than the Γ_{e-hh}, the transport behaviors of electrons and holes at forwarding injection conditions also affect the radiative and nonradiative recombination as well as the spontaneous emission rates of DUV LEDs. Figure 4(a) presents the electron distribution within the active region of the four devices. With embedded $p-i-n$ junctions in the active region, boosted electron concentration can be observed in the first four QWs for Devices B to D compared to Device A. However, in the last QW, the electron concentration of Device A is the highest among the four devices.

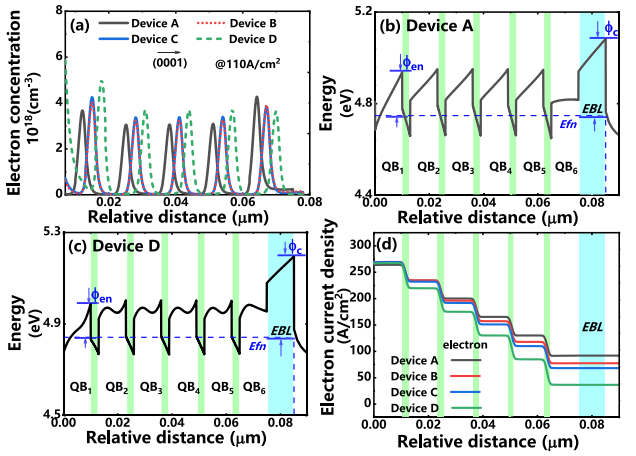

Fig. 4. (a) Electron concentration profiles. The conduction band of (b) Device A and (c) Device D in the MQWs; (d) electron current density. The data are extracted at the injection current density of 110 A/cm^2. Note that since the conduction band structures of Device B and Device C are similar to that of Device D, the band diagrams of Device B and C are not presented.

Table 1. Values of Φ_{en} for Devices A, B, C, and D

Φ (meV)	Device A	Device B	Device C	Device D
Φ_{e1}	188.77	171.56	168.27	146.74
Φ_{e2}	202.65	186.78	184.05	161.19
Φ_{e3}	202.74	186.78	184.04	161.17
Φ_{e4}	202.62	186.69	183.95	161.04
Φ_{e5}	199.79	184.96	182.72	159.57
Φ_c	340.03	345.50	348.95	358.51

To explain the distribution of electrons in the QWs, we compared the conduction band of Devices A and D, as shown in Figs. 4(b) and 4(c), and extracted the conduction band barrier height of each QB, which is one of the determining factors for the electron transport behavior. The potential barrier heights for electrons in the EBL (symbolized as Φ_c) and QBs (symbolized as Φ_{en}) are defined as the energy difference between the highest point of the conduction band and the quasi-Fermi levels for electrons, values of which are displayed in Table 1. The values of Φ_{en} in each QB decrease monotonously from Device A to Device D, which indicates that the Si doping in the embedded $p-i-n$ junctions can effectively decrease the effective barrier height for electrons and favor the electron injection into the active region. Moreover, the lower electron concentration recorded in the last QW of Device D can be attributed to the fact that the ionized Mg impurities act as negative charge centers, which can reflect electrons back to the first four QWs and reduce the electron overflow to the p-type region.

As shown in Fig. 4(d), the lowest leakage level of the electron can be observed in Device D. The alleviated electron leakage can be partly attributed to the increased Φ_c in Device D. In addition, the rates of different recombination events in the MQWs of Device D are higher than those of Device A, indicating that more electrons can be consumed in the active region instead of overflowing into the p-type region. Hence, the electron leakage is efficiently suppressed with the combined impact of increased

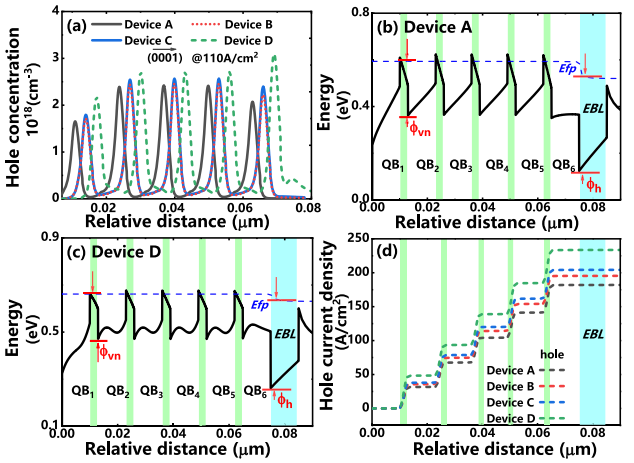

Fig. 5. (a) Hole concentration profiles; valence band of (b) Device A and (c) Device D in the MQWs; (d) hole current density. The data are extracted at the injection current density of 110 A/cm^2. Note that since the valance band structures of Device B and Device C are similar to that of Device D, the band diagrams of Device B and C are not presented.

Table 2. Values of Φ_{en} for Devices A, B, C, and D

Φ (meV)	Device A	Device B	Device C	Device D
Φ_{v2}	231.35	216.11	213.12	189.91
Φ_{v3}	228.91	214.23	211.48	190.38
Φ_{v4}	228.94	214.29	211.54	190.41
Φ_{v5}	229.20	214.42	211.61	190.50
Φ_h	466.70	446.18	435.85	398.75

Φ_c and enhanced recombination, which can lead to reduced nonradiative recombination in the p-type region.

Different from the electron distribution, the hole concentration in the QWs increases sequentially from Device A to Device D, as shown in Fig. 5(a). Similarly, the valence bands of Device A and Device D are displayed in Figs. 5(b) and 5(c). And the potential barrier heights for holes in the EBL (symbolized as Φ_h) and QBs (symbolized as Φ_{vn}) are also displayed in Table 2, which are defined as the energy difference between the lowest point of the valence band and the quasi-Fermi levels for holes, respectively.

The values of Φ_{vn} in each QB monotonously decrease from Device A to Device D, which suggests that the Mg doping in the QB region adjacent to QW can facilitate the decrease of the barrier height for holes at the QB/QW interface. Therefore, the hole concentration in the QWs is enhanced correspondingly in the proposed devices with embedded $p-i-n$ junctions. The Φ_h of the four devices also shows a decreasing trend from Device A to Device D. The lowest Φ_h of 398.75 meV leads to the best hole injection capability in Device D, as shown in Fig. 5(d).

Therefore, Device D exhibits the optimum electron and hole distribution profiles in the active region, which can contribute to the highest radiative recombination rates according to the ABC model [44–46].

4. CONCLUSION

In conclusion, we propose an alternative approach to alleviate the built-in electric field in the active region for the purpose of enhancing the LOP and EQE of DUV LEDs. By taking advantage of the reversely orientated electric field induced by the ionized dopants from the embedded $p-i-n$ junctions at the vicinity of the QWs, the polarization-induced electric field can be effectively compensated, resulting in remarkably enhanced overlap of the hole and electron wave functions and thus, improved radiative recombination efficiency. The influence of the embedded $p-i-n$ junctions on the band diagram structure and carrier transport behavior is also investigated systematically by adapting different doping thicknesses and concentrations. We believe that our proposed DUV LEDs with embedded $p-i-n$ junction provide an effective approach to obtain efficient DUV LEDs.

Funding. Natural Science Foundation of Shandong Province (ZR2020QF079); Shenzhen Science and Technology Innovation Program (GJHZ20210705142537002, JCYJ20210324141212030); Basic and Applied Basic Research Foundation of Guangdong Province (2020A1515111018); Qilu Young Scholar program (11500089963075).

Disclosures. The authors declare no conflicts of interest.

Data availability. Data underlying the results presented in this paper are not publicly available at this time but may be obtained from the authors upon reasonable request.

REFERENCES

1. K. Song, M. Mohseni, and F. Taghipour, "Application of ultraviolet light-emitting diodes (UV-LEDs) for water disinfection: a review," Water Res. **94**, 341–349 (2016).
2. D. B. Li, K. Jiang, X. J. Sun, and C. L. Guo, "AlGaN photonics: recent advances in materials and ultraviolet devices," Adv. Opt. Photon. **10**, 43–110 (2018).
3. A. Khan, K. Balakrishnan, and T. Katona, "Ultraviolet light-emitting diodes based on group three nitrides," Nat. Photonics **2**, 77–84 (2008).
4. M. Kneissl, T. Y. Seong, J. Han, and H. Amano, "The emergence and prospects of deep-ultraviolet light-emitting diode technologies," Nat. Photonics **13**, 233–244 (2019).
5. H. B. Yu, M. H. Memon, D. H. Wang, Z. J. Ren, H. C. Zhang, C. Huang, M. Tian, H. D. Sun, and S. B. Long, "AlGaN-based deep ultraviolet micro-LED emitting at 275 nm," Opt. Lett. **46**, 3271–3274 (2021).
6. Y. K. Kuo, J. Y. Chang, F. M. Chen, Y. H. Shih, and H. T. Chang, "Numerical investigation on the carrier transport characteristics of AlGaN deep-UV light-emitting diodes," IEEE J. Quantum Electron. **52**, 3300105 (2016).
7. M. L. Nakarmi, K. H. Kim, M. Khizar, Z. Y. Fan, J. Y. Lin, and H. X. Jiang, "Electrical and optical properties of Mg-doped $Al_{0.7}Ga_{0.3}N$ alloys," Appl. Phys. Lett. **86**, 092108 (2005).
8. F. Mehnke, C. Kuhn, M. Guttmann, C. Reich, T. Kolbe, V. Kueller, A. Knauer, M. Lapeyrade, S. Einfeldt, J. Rass, T. Wernicke, M. Weyers, and M. Kneissl, "Efficient charge carrier injection into sub-250 nm AlGaN multiple quantum well light emitting diodes," Appl. Phys. Lett. **105**, 051113 (2014).
9. J. Y. Chang, H. T. Chang, Y. H. Shih, F. M. Chen, M. F. Huang, and Y. K. Kuo, "Efficient carrier confinement in deep-ultraviolet light-emitting diodes with composition-graded configuration," IEEE Trans. Electron Devices **64**, 4980–4984 (2017).
10. Z. H. Zhang, S. W. H. Chen, Y. H. Zhang, L. P. Li, S. W. Wang, K. K. Tian, C. S. Chu, M. Q. Fang, H. C. Kuo, and W. G. Bi, "Hole transport manipulation to improve the hole injection for deep ultraviolet light-emitting diodes," ACS Photon. **4**, 1846–1850 (2017).
11. Z. H. Zhang, J. Q. Kou, S. W. H. Chen, H. Shao, J. M. Che, C. S. Chu, K. K. Tian, Y. H. Zhang, W. G. Bi, and H. C. Kuo, "Increasing the hole

energy by grading the alloy composition of the p-type electron blocking layer for very high-performance deep ultraviolet light-emitting diodes," Photon. Res. **7**, B1–B6 (2019).
12. Z. L. Liu, H. B. Yu, Z. J. Ren, J. N. Dai, C. Q. Chen, and H. D. Sun, "Polarization-engineered AlGaN last quantum barrier for efficient deep-ultraviolet light-emitting diodes," Semicond. Sci. Technol. **35**, 075021 (2020).
13. L. Lu, X. Zhang, S. C. Wang, A. J. Fan, S. Chen, C. Li, A. Nasir, Z. Zhuang, G. H. Hu, and Y. P. Cui, "Impact of composite last quantum barrier on the performance of AlGaN-based deep ultraviolet light-emitting diode," J. Mater. Sci. Mater. Electron. **32**, 18138–18144 (2021).
14. S. L. Wang, Y. A. Yin, H. M. Gu, N. Y. Wang, and L. Liu, "Graded AlGaN/AlGaN superlattice insert layer improved performance of AlGaN-based deep ultraviolet light-emitting diodes," J. Disp. Technol. **12**, 1112–1116 (2016).
15. C. S. Chu, K. K. Tian, J. M. Che, H. Shao, J. Q. Kou, Y. H. Zhang, Y. Li, M. Y. Wang, Y. H. Zhu, and Z. H. Zhang, "On the origin of enhanced hole injection for AlGaN-based deep ultraviolet light-emitting diodes with AlN insertion layer in p-electron blocking layer," Opt. Express **27**, A620–A628 (2019).
16. M. R. Liu, Y. C. Ji, H. Zhou, C. S. Xia, Z. H. Zhang, and C. Liu, "Sheet charge engineering towards an efficient hole injection in 290 nm deep ultraviolet light-emitting diodes," IEEE Photon. J. **13**, 8200308 (2021).
17. H. Hirayama, T. Yatabe, N. Noguchi, T. Ohashi, and N. Kamata, "231–261 nm AlGaN deep-ultraviolet light-emitting diodes fabricated on AlN multilayer buffers grown by ammonia pulse-flow method on sapphire," Appl. Phys. Lett. **91**, 071901 (2007).
18. T. Mino, H. Hirayama, T. Takano, N. Noguchi, and K. Tsubaki, "Highly uniform 260 nm-band AlGaN-based deep-ultraviolet light-emitting diodes developed by 2-inch×3 MOVPE system," Phys. Status Solidi C **9**, 749–752 (2012).
19. N. Roccato, F. Piva, C. De Santi, R. Brescancin, K. Mukherjee, M. Buffolo, C. Haller, J. F. Carlin, N. Grandjean, M. Vallone, A. Tibaldi, F. Bertazzi, M. Goano, G. Verzellesi, G. Meneghesso, E. Zanoni, and M. Meneghini, "Modeling the electrical characteristics of InGaN/GaN LED structures based on experimentally-measured defect characteristics," J. Phys. D **54**, 425105 (2021).
20. F. Piv, C. De Santi, A. Caria, C. Haller, J. F. Carlin, M. Mosca, G. Meneghesso, E. Zanoni, N. Grandjean, and M. Meneghini, "Defect incorporation in in-containing layers and quantum wells: experimental analysis via deep level profiling and optical spectroscopy," J. Phys. D **54**, 025108 (2021).
21. N. Roccato, F. Piva, C. De Santi, M. Buffolo, C. Haller, J. F. Carlin, N. Grandjean, G. Meneghesso, E. Zanoni, and M. Meneghini, "Effects of quantum-well indium content on deep defects and reliability of InGaN/GaN light-emitting diodes with under layer," J. Phys. D **54**, 505108 (2021).
22. J. Brault, D. Rosales, B. Damilano, M. Leroux, A. Courville, M. Korytov, S. Chenot, P. Vennegues, B. Vinter, P. De Mierry, A. Kahouli, J. Massies, T. Bretagnon, and B. Gil, "Polar and semipolar GaN/$Al_{0.5}Ga_{0.5}N$ nanostructures for UV light emitters," Semicond. Sci. Technol. **29**, 084001 (2014).
23. Z. H. Zhang, K. K. Tian, C. S. Chu, M. Q. Fang, Y. H. Zhang, W. G. Bi, and H. C. Kuo, "Establishment of the relationship between the electron energy and the electron injection for AlGaN based ultraviolet light-emitting diodes," Opt. Express **26**, 17977–17987 (2018).
24. H. B. Yu, Z. J. Ren, H. C. Zhang, J. N. Dai, C. Q. Chen, S. B. Long, and H. D. Sun, "Advantages of AlGaN-based deep-ultraviolet light-emitting diodes with an Al-composition graded quantum barrier," Opt. Express **27**, A1544–A1553 (2019).
25. M. M. Satter, Z. Lochner, J. H. Ryou, S. C. Shen, R. D. Dupuis, and P. D. Yoder, "Polarization matching in AlGaN-based multiple-quantum-well deep ultraviolet laser diodes on AlN substrates using quaternary AlInGaN barriers," J. Lightwave Technol. **30**, 3017–3025 (2012).
26. H. D. Sun, S. Mitra, R. C. Subedi, Y. Zhang, W. Guo, J. C. Ye, M. K. Shakfa, T. K. Ng, B. S. Ooi, I. S. Roqan, Z. H. Zhang, J. N. Dai, C. Q. Chen, and S. B. Long, "Unambiguously enhanced ultraviolet luminescence of AlGaN wavy quantum well structures grown on large misoriented sapphire substrate," Adv. Funct. Mater. **29**, 1905445 (2019).
27. K. K. Tian, Q. Chen, C. S. Chu, M. Q. Fang, L. P. Li, Y. H. Zhang, W. G. Bi, C. Q. Chen, Z. H. Zhang, and J. N. Dai, "Investigations on AlGaN-based deep-ultraviolet light-emitting diodes with Si-doped quantum barriers of different doping concentrations," Phys. Status Solidi RRL **12**, 1700346 (2018).
28. W. Liu, S. W. Yuan, and X. Y. Fan, "Leakage of holes induced by Si doping in the AlGaN first barrier layer in GaN/AlGaN multiple-quantum-well ultraviolet light-emitting diodes," J. Lumin. **231**, 117806 (2021).
29. http://www.crosslight.com/.
30. I. Vuraftman and J. R. Meyer, "Band parameters for nitrogen-containing semiconductors," J. Appl. Phys. **94**, 3675–3696 (2003).
31. V. Fioentini, F. Bernardini, and O. Ambacher, "Evidence for nonlinear macroscopic polarization in III-V nitride alloy heterostructures," Appl. Phys. Lett. **80**, 1204–1206 (2002).
32. F. Z. Li, L. S. Wang, G. J. Zhao, Y. L. Meng, H. J. Li, S. Y. Yang, and Z. G. Wang, "Performance enhancement of AlGaN-based ultraviolet light-emitting diodes by inserting the last quantum well into electron blocking layer," Superlattices Microstruct. **110**, 324–329 (2017).
33. Y. Kang, H. B. Yu, Z. J. Ren, C. Xing, Z. L. Liu, H. F. Jia, W. Guo, and H. D. Sun, "Efficiency droop suppression and light output power enhancement of deep ultraviolet light-emitting diode by incorporating inverted-V-shaped quantum barriers," IEEE Trans. Electron Devices **67**, 4958–4962 (2020).
34. C. Xing, H. B. Yu, Z. J. Ren, H. C. Zhang, J. N. Dai, C. Q. Chen, and H. D. Sun, "Performance improvement of AlGaN-based deep ultraviolet light-emitting diodes with step-like quantum barriers," IEEE J. Quantum Electron. **56**, 3300106 (2020).
35. F. M. Chen, M. F. Huang, J. Y. Chang, and Y. K. Kuo, "Effects of number of quantum wells and Shockley–Read-Hall recombination in deep-ultraviolet light-emitting diodes," Opt. Lett. **45**, 3749–3752 (2020).
36. J. Piprek, "Ultra-violet light-emitting diodes with quasi acceptor-free AlGaN polarization doping," Opt. Quantum Electron. **44**, 67–73 (2012).
37. D. Y. Zhang, C. S. Chu, K. K. Tian, J. Q. Kou, W. G. Bi, Y. H. Zhang, and Z. H. Zhang, "Improving hole injection from p-EBL down to the end of active region by simply playing with polarization effect for AlGaN based DUV light-emitting diodes," AIP. Adv. **10**, 065032 (2020).
38. E. Kioupakis, Q. M. Yan, and C. G. Van de Walle, "Interplay of polarization fields and Auger recombination in the efficiency droop of nitride light-emitting diodes," Appl. Phys. Lett. **101**, 231107 (2012).
39. M. Deppner, F. Römer, and B. Witzigmann, "Auger recombination and carrier transport effects in III-nitride quantum well light emitting diodes," Proc. SPIE **8619**, 86191J (2013).
40. J. Y. Chang, B. T. Liou, M. F. Huang, Y. H. Shih, F. M. Chen, and Y. K. Kuo, "High-efficiency deep-ultraviolet light-emitting diodes with efficient carrier confinement and high light extraction," IEEE Trans. Electron Devices **66**, 976–982 (2019).
41. M. Shatalov, J. W. Yang, W. H. Sun, R. Kennedy, R. Gaska, K. Liu, M. Shur, and G. Tamulaitis, "Efficiency of light emission in high aluminum content AlGaN quantum wells," J. Appl. Phys. **105**, 073103 (2009).
42. P. Dong, J. C. Yan, Y. Zhang, J. X. Wang, C. Geng, H. Y. Zheng, X. C. Wei, Q. F. Yan, and J. M. Li, "Optical properties of nanopillar AlGaN/GaN MQWs for ultraviolet light-emitting diodes," Opt. Express **22**, A320–A327 (2014).
43. Z. Zhuang, D. Iida, and K. Ohkawa, "Effects of size on the electrical and optical properties of InGaN-based red light-emitting diodes," Appl. Phys. Lett. **116**, 173501 (2020).
44. S. Karpov, "ABC-model for interpretation of internal quantum efficiency and its droop in III-nitride LEDs: a review," Opt. Quantum Electron. **47**, 1293–1303 (2015).
45. M. A. Hopkins, D. W. E. Allsopp, M. J. Kappers, R. A. Oliver, and C. J. Humphreys, "The ABC model of recombination reinterpreted: impact on understanding carrier transport and efficiency droop in InGaN/GaN light emitting diodes," J. Appl. Phys. **122**, 234505 (2017).
46. W. G. Scheibenzuber, U. T. Schwarz, L. Sulmoni, J. Dorsaz, J. F. Carlin, and N. Grandjean, "Recombination coefficients of GaN-based laser diodes," J. Appl. Phys. **109**, 093106 (2011).